Geophysical Journal International

Geophys. J. Int. (2012) **189,** 357–368 doi: 10.1111/j.1365-246X.2012.5385.x

Approximations for the 2-D coast effect on marine magnetotelluric data

Tamara Worzewski,* Marion Jegen and Andrei Swidinsky

GEOMAR Helmholtz Centre for Ocean Research Kiel, Wischhofstrasse 1-3, 24148 *Kiel, Germany. E-mail: tworzewski@bam.de*

Accepted 2012 January 11. Received 2011 December 15; in original form 2010 December 16

SUMMARY

Marine natural source electromagnetic data acquired on continental margins are often of considerable scientific and commercial interest. However, the large conductivity contrast between the ocean and coast causes this type of data to be severely distorted. For a 2-D coastal model, this distortion is most pronounced for the marine magnetotelluric and geomagnetic response function derived from induced currents flowing parallel to the coast. A maximal distortion occurs for a given period at a specific distance from the coast and causes severe anomalies in the magnitude and phase of the response functions. Based on a modelling study, we empirically relate the characteristic period and characteristic distance to physical parameters such as the ocean depth and the host resistivity. Based on a simple analytical approach, we test these approximations and show that maximum distortion occurs when destructive interference between the ocean and host response is at its highest. While the coast effect causes a large distortion in the marine responses we show through a resolution analysis that it does not mask subsurface conductivity anomalies but in fact increases the sensitivity to the seafloor.

Key words: Electromagnetic theory; Magnetotelluric; Magnetic anomalies: modelling and interpretation; Magnetic field; Marine electromagnetics.

1 INTRODUCTION

In a joint cooperation between the Free University of Berlin and GEOMAR in 2007–2008 an on- and offshore magnetotelluric (MT) survey was conducted in Costa Rica. The aim of this study was to image enhanced conductivity anomalies associated with fluids in a subduction zone. We recorded curious effects in the responses offshore, which would be considered unusual on land. Peaks occurred in the Transverse Electric (TE) mode apparent resistivity curves, which were accompanied by phases that systematically progressed through all four quadrants. At the same time, the magnetic transfer function (also called the Tipper) increased to extremely high values. However, the Transverse Magnetic (TM) mode apparent resistivities were less affected (for map see Fig. 1 and for data see Fig. 2). The unusual responses made it challenging to invert the data to produce an electrical resistivity model, requiring a systematic analysis of these effects. Although the Costa Rican experiment was successful (Worzewski *et al.* 2011), various outstanding questions remained:

(1) What is the nature of the pronounced distortion in the TE mode and Tipper?

(2) Are these curves physically meaningful or would the pronounced distortion possibly hamper the detection of subsurface conductivity anomalies?

(3) Can these curves easily be used in 2-D inversions?

*Now at: BAM Federal Institute for Materials Research and Testing, 12200 Berlin, Germany.

Comparable data have been recorded and modelled previously. In the framework of the Tasman Project, Ferguson (1988), Ferguson *et al.* (1990) and Heinson & Lilley (1993) evaluate marine MT recordings between the Australian and the New Zealand shores. Ferguson (1988) records anomalously high Tipper values expressed by induction arrows and observes a frequency-dependence of anomalous offshore Tipper magnitudes. Furthermore, the TE mode phases of some stations in the Tasman Sea systematically progress through all four quadrants and the TE mode apparent resistivities show extreme values at specific periods (Lilley *et al.* 1989). Although the investigation of Ferguson *et al.* (1990) indicates that the geomagnetic induction is influenced by the large-scale 3-D conductivity structure of the region, Ferguson (1988) had already recognized that the most pronounced features may be attributed simply to a 2-D coastal effect. These results were subsequently confirmed by modelling studies of Kellet *et al.* (1991).

Analysis of TE mode distortions was not addressed systematically until negative phases and peaks were reported offshore California by Constable *et al.* (2009). They were able to qualitatively reproduce these special features with a 2-D bathymetric model and found that the distortion in the TE mode depends on the host resistivity. Alekseev *et al.* (2009) also modelled TE mode apparent resistivities peaks and phases that systematically progress through all four quadrants. These particular resistivity peaks and anomalous phases have also been observed in real data offshore the Nicaraguan subduction zone (Naif *et al.* 2010), and also offshore the San Andreas Fault in California (Wheelock *et al.* 2010). Currently, coast-distorted marine curves are taken into account for the

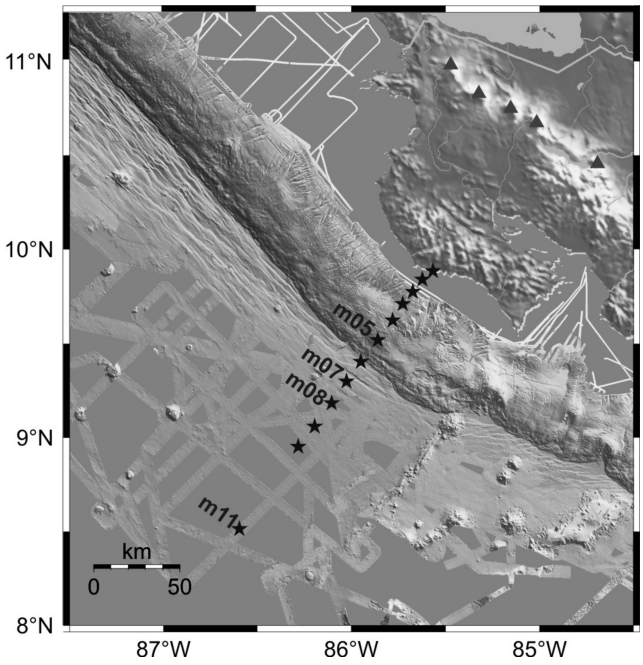

Figure 1. The marine profile offshore Costa Rica.

inversion processes and can be well fitted, as has been presented by Constable *et al.* (2009), Wheelock *et al.* (2010), Naif *et al.* (2010) and also of the Costa Rican data set (Worzewski *et al.* 2011). However, a quantitative analysis of the distortion was still lacking.

We will investigate the special nature of the responses in the TE mode and Tipper by a comprehensive modelling study. Our aim is to quantitatively evaluate the parameters that control the coast effect and to investigate whether the distorted responses contain any useful geological information. A previous modelling study resulted in the derivation of characteristic relationships between these parameters (Worzewski & Jegen-Kulcsar 2010), and our findings are evaluated here in detail. The marine coast effect and the specific shapes in the marine transfer functions are a timely subject, which becomes obvious by a recent study of Key & Constable (2011). This latter paper also reports on distorted data offshore Japan, and empirically derive similar characteristic approximations—independently of us and using a different approach. In this study, our characteristic approximations will be thoroughly discussed and compared to the findings of Key & Constable (2011). In addition, we will present a simple physical explanation for these approximations based on the theory of induction numbers. This study will also show that the coast effect can help with data interpretation as it contains information regarding the average host resistivity and increases the sensitivity to conductivity anomalies. Furthermore, it will be shown that marine data which is distorted by the coast effect can be used effectively when the coastline is directly implemented into the inversion process.

It should be mentioned that one must distinguish between bathymetric and coastal effects on marine MT responses. Bathymetric effects on MT data are well understood (e.g. Schwalenberg & Edwards 2004), and might even be removed from the data (e.g. Nolasco *et al.* 1998; Baba & Seama 2002; Baba & Chave 2005). However, at this time, the coast effect cannot be removed easily, because the coastal distortion is coupled to the unknown subsurface resistivity, as will be shown in this study. Baba & Chave (2005) use an iterative topographic stripping method that depends on the underlying resistivity model and can include the coast. Yet, for complicated ocean-coast scenarios with 2-D or 3-D features, it is difficult to distinguish what portion of the data should be removed and what contains information on subsurface resistivity features.

2 COASTAL DISTORTION IN TE MODE AND TIPPER RESPONSES

MT measurements recorded offshore in Costa Rica are depicted in Fig. 2. Station m05 (right-hand column) was located on the continental slope 50 km offshore. Stations m07 and m08 (middle columns) were further offshore (80 and 95 km from the coast) whereas station m11 (left-hand column) was farthest from the coast (190 km offshore). Some stations, including m07 and m08, have

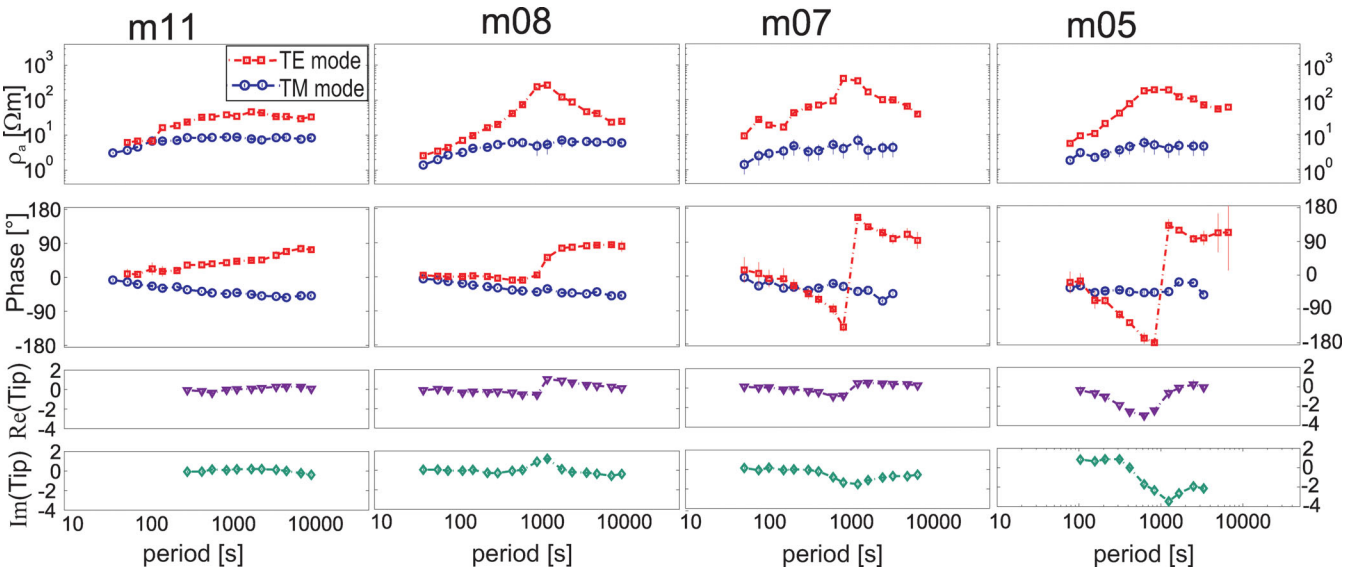

Figure 2. Response functions of selected marine stations. Uppermost panels: Apparent resistivities; middle panels: Phases (scaling from −180° to +180°); lower two panels: real and imaginary components of the Tipper transfer function. Please note that, for simplicity, TE phases were mirrored on the *x*-axis (multiplication by −1). Station names refer to Fig. 1.

pronounced peaks in the TE mode apparent resistivities at periods around 1000 s. The TE mode phases of m07, m05 and m04 systematically progress through all four quadrants.

Tipper values of stations m04–m08 exceed typical values (i.e. they are greater than unity) and taper off at around 1000 s. We give our exact definition of the Tipper in Appendix. Additionally, the peak in the imaginary part of the Tipper changes polarity between m08 and m07. As we will see, these abnormal responses may be attributed to the presence of the coast.

To attempt to understand these data, we perform a comprehensive modelling study using the 2-D finite element code 'FEMMT' developed by Franke *et al.* (2007). FEMMT uses an adaptive unstructured triangular grid, which is suitable for simulating electromagnetic fields on the ocean bottom. This is because unstructured grids can closely conform to seafloor bathymetry. Marine MT responses are calculated in a simple coastal setting with a continental slope as shown in Fig. 3(a). Note that TE mode here refers to a 2-D situation with the profile oriented perpendicular to the coast (such

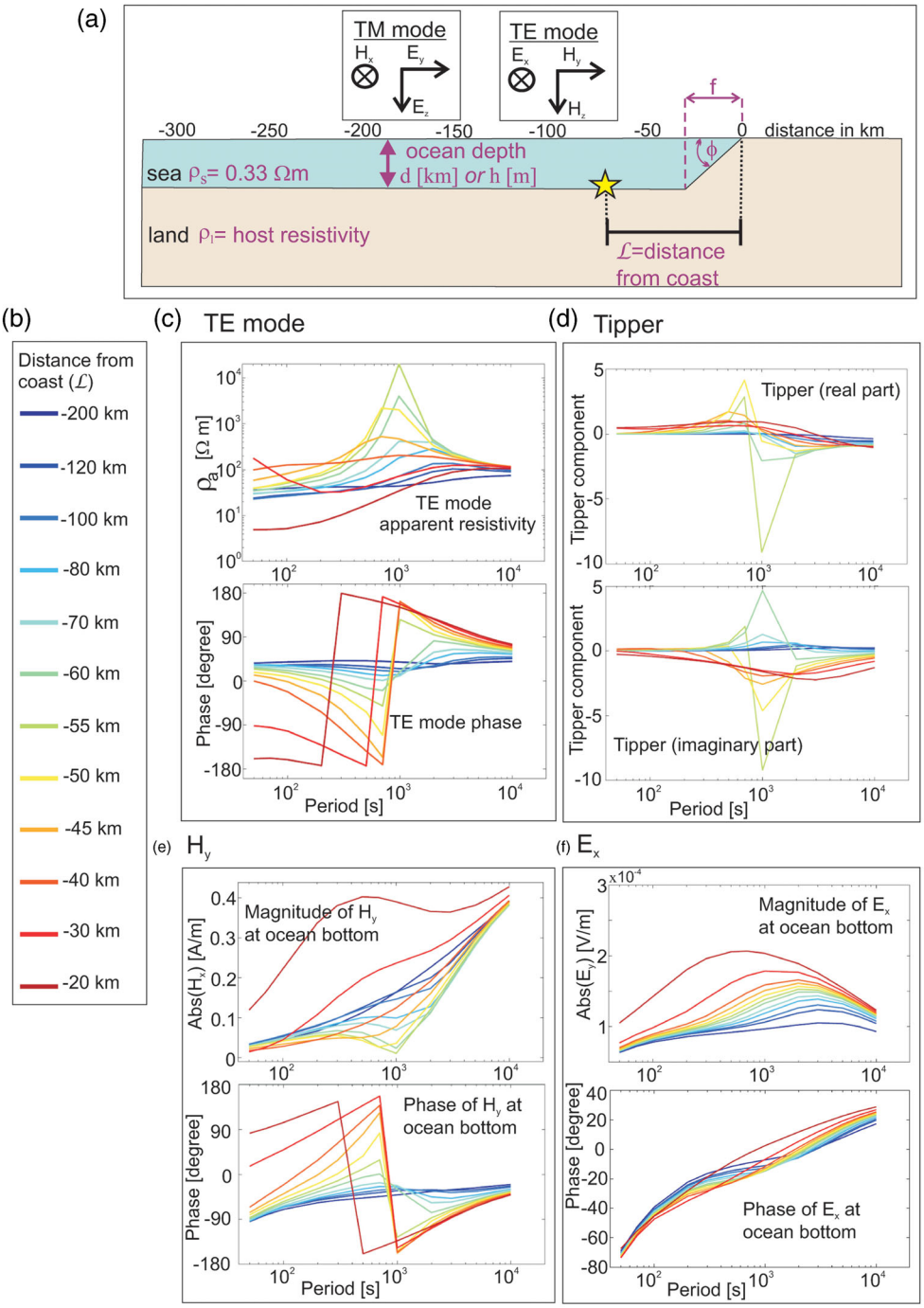

Figure 3. Modelled transfer functions and electromagnetic field components of selected stations on ocean bottom for a fixed ocean depth (4 km) and a fixed background resistivity (50 Ωm); the model is shown in (a). (c)–(f) display responses of the TE mode, Tipper, and magnetic and electric fields at the ocean bottom. The periods on the *x*-axes are scaled between 40 and 10 000 s. Each coloured curve is the response of a station at a certain distance to the coast [legend in (b)].

that the TE mode features are parallel to the shore). The subseafloor resistivity is set to 50 Ωm and the ocean depth to 4 km, values which can be regarded as average for subduction zones. The full model in this case extends from −800 to +800 km horizontally and down to 600 km depth. The coast in this model is located at the origin. An appropriate mesh adapted to the station position, the conductivity contrast and the model geometry is generated automatically within FEMMT.

The TE mode and Tipper responses for several seafloor stations are displayed in different colours in Figs 3(c)–(f). Stations far away from the coast (blue curves) show normal responses for periods up to a few thousand seconds. The coast effect produces increased TE mode apparent resistivities at longer periods, where the skin depth of the host becomes large. Close to the coast, we observe this increase in apparent resistivity in the form of peaks at progressively smaller periods. In this particular setting, the most pronounced peak (defined as having the smallest half-width and the greatest magnitude) is observed at the station at around 55 km distance from the coast (green curve) at a period of around 1000 s (Fig. 3b). At the same distance and period, phases leave the quadrant and Tipper responses increase dramatically (Fig. 3c). Stations closer to the coast display decreasing peaks in the TE mode apparent resistivities and decreasing Tipper values. Similar distortion has been observed previously by Alekseev *et al.* (2009).

In this paper, we shall refer to this abnormal effect on the apparent resistivity (most pronounced peak), Tipper (highest values) and phase (starting to move out of quadrant) as the 'maximum coast effect'. $\mathcal{T}$ shall denote the characteristic period and $\mathcal{L}$ the characteristic distance to the coast at which this maximum coast effect occurs.

As can be seen in Fig. 3(e), the maximum coast effect is related to a minimum in the magnitude of the horizontal magnetic field component $\mathbf{H}_y$. A minimum in field strength occurs at exactly the location of the maximum coast effect (green curve). In contrast, the horizontal electric field (Fig. 3e) does not display any anomalous behaviour at this location. As a result, in calculations of both the impedance and the Tipper, it is the minimum in the magnetic field which results in a maximum in apparent resistivity and Tipper.

3 WHY IS THERE A MINIMUM IN THE HORIZONTAL MAGNETIC FIELD?

Constable *et al.* (2009) describe the TE mode distortion as an 'inductive effect associated with currents flowing along the edge of the deep ocean basins, steepening the magnetic field and even causing a phase reversal in the horizontal field used for MT impedance calculations (and thus generating negative phases)'.

We investigate this statement by calculating the electromagnetic field in both the ocean and the host half-space. Figs 4(a)–(d) displays the current density $\mathbf{j}_x$ (parallel to the coastline, pointing into the paper plane) and Figs 4(e)–(h) the horizontal magnetic field $\mathbf{H}_y$(perpendicular to the coast line) all at 1000 s. These fields are expressed by both their real and imaginary components, and by their magnitude and phase. In Fig. 4, the pink star denotes the position on the ocean bottom at which the maximum coast effect occurs.

The minimum in the magnitude of the magnetic field $|\mathbf{H}_y|$ (producing the maximum coast effect) is accompanied by a rapid phase change (Fig. 4h). Stations between the star and the coast observe phases that occur in all four quadrants. The amplitude of the current density is strongest at the edge of the coast (see Fig. 4c). However, the phase of the complex valued current density changes within the water column above the star in Fig. 4(d). This suggests the presence of an anomalous current flowing above the position of the maximum coast effect. The anomalous current can be seen in the imaginary components of the magnetic field (Fig. 4e) and the current density (Fig. 4a). The magnitude of the current density is highest at the edge of the coast. However, the imaginary component becomes negative in the vicinity of the star. This suggests a pronounced change in the induced current pattern. We infer from this directional change of current density and magnetic field that an anomalous current is flowing above the star. However, this effect is small in comparison to the increased current flow at the edge, but has a large impact on the response due to its proximity to the station.

4 DEFINITION OF A CHARACTERISTIC LENGTH AND PERIOD

Constable *et al.* (2009) perform modelling studies for a simple ocean-coast setting and calculate the MT response for varying host resistivities. At one seafloor station, they observe that the cusp in the TE mode apparent resistivity vanishes for a change in host resistivity. We extend this study and show that the location of this effect is dependent on host resistivity and ocean depth; in fact, it never vanishes, but rather 'moves'. In the following sections, we shall introduce some approximations to describe these relations.

Varying the host resistivity and depth changes the position and also the period at which the maximum coast effect is detected. This is also indirectly observed in real data from the Tasman Project; Ferguson (1988) demonstrated that the Tipper magnitudes became highest at certain distances from the coast; these distances vary with period. In particular, the maximum in response appears to move away from the coast at longer periods, which Ferguson (1988) explains by the gradually deepening ocean.

We calculate several sets of models and vary physical parameters such as the ocean depth d (from 100 m to 8 km), the host (land half-space) resistivity ρ_l (from 50 to 1000 Ωm) and the angle of the continental slope, using the code of Rodi & Mackie (2001). The ocean resistivity is fixed to 0.33 Ωm (the average resistivity of sea water). The model extent is dependent on the host resistivity and is adapted accordingly. To exclude boundary effects, each model was tested by extending its size horizontally and vertically and was regarded as sufficiently wide if no differences in the calculated responses were observed. The advantages of the unstructured grid in FEMMT are not necessary here as the test models are constructed without topography. The reason for choosing the finite difference code of Rodi & Mackie (2001) over the finite element code of Franke *et al.* (2007) is only because of an increased calculation speed.

Our observations for models with a vertical slope are given in Table 1. Further information on the models can be found in the table's caption. Using these results, we shall attempt to approximate a characteristic period $\mathcal{T}$ and a characteristic distance to the coast $\mathcal{L}$, at which the maximum coast effect may be expected. Responses for all models are calculated with 20 periods per decade to allow $\mathcal{T}$ to be precisely determined. The uncertainty in the detection of the characteristic period is determined by the length of the interval to the next calculated period. As the difference between two neighbouring periods equals 10 per cent, the error in the observed period is likewise estimated at 10 per cent.

For a vertical coast, that is, for a continental slope angle of $\phi = 90^\circ$ (nomenclature of Fig. 3a), we found the following dependencies from a exponential fit of the data in Table 1:

$$\mathcal{L} \approx 0.2 \cdot \sqrt{\rho_l \cdot \mathcal{T}}, \tag{1}$$

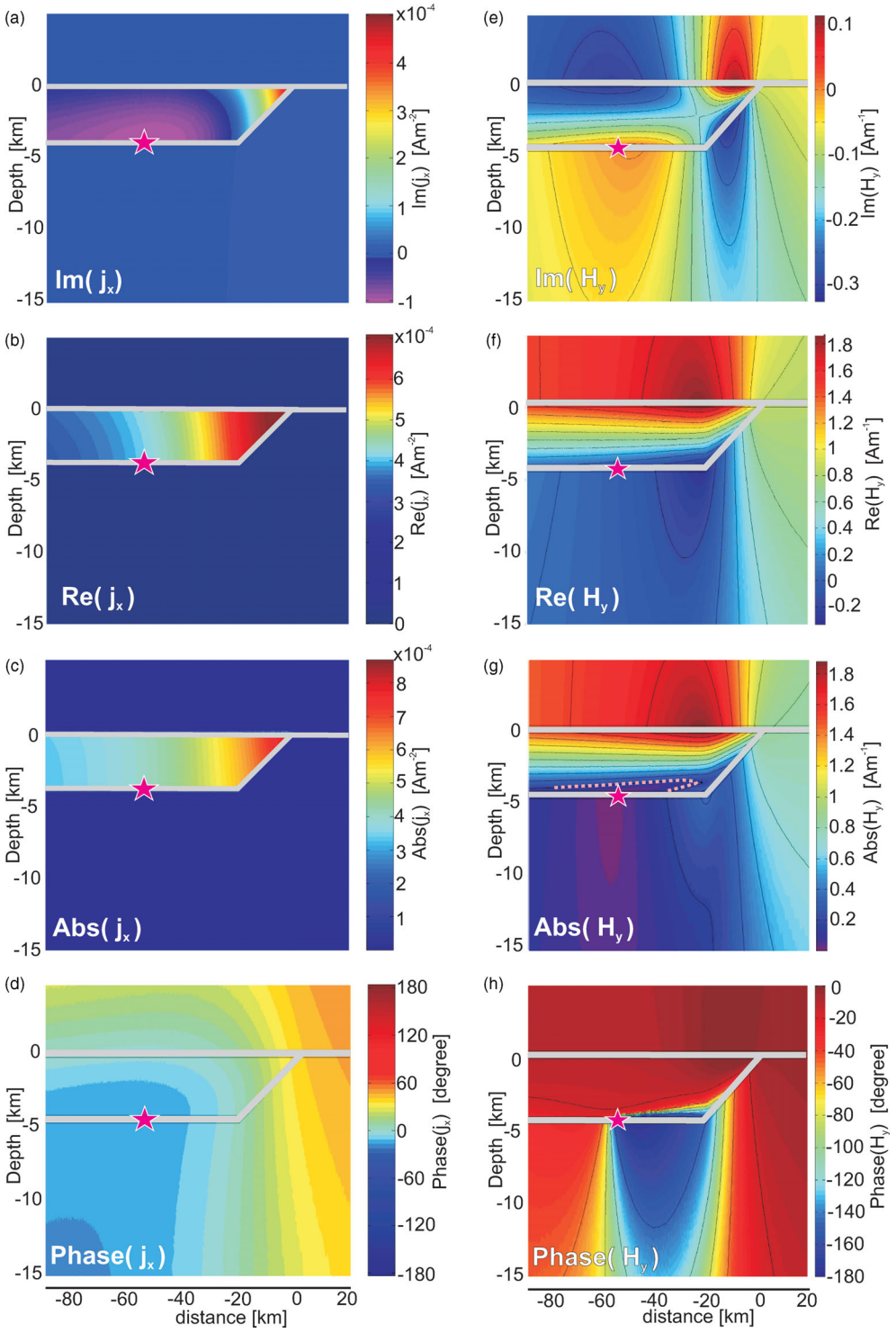

Figure 4. Field components of complex current density $\mathbf{j}_x$ in the Earth for the TE mode (pointing into the paper plane, left-hand column) and complex valued horizontal magnetic field $\mathbf{H}_y$ (pointing towards the coast, right-hand column) at 1000 s (period of the maximum coast effect in this model). Complex values are expressed both through real (Re) and imaginary (Im) modulus and by magnitude (Abs) and phase. The star denotes the position at which the maximum coast effect is observed. Note that the Tipper is dimensionless. Also note that *d* represents ocean depth in kilometres and *h* represents ocean depth in metres.

$$\mathcal{T} \approx 3 \cdot \rho_1^{0.9} \cdot d^2, \tag{2}$$

where $\mathcal{L}$ is measured in (km), $\mathcal{T}$ in (s), d in (km) and ρ_1 in (Ωm).

Substituting eq. (2) into eq. (1) yields

$$\mathcal{L} \approx 0.35 \cdot \rho_1^{0.95} \cdot d. \tag{3}$$

It should be noted that the ocean resistivity was fixed to 0.33 Ωm (the average resistivity of sea water).

Fig. 5 shows the comparison between the observed distances in Table 1 with the calculated distances of eq. (1). The deviation between the observed and calculated distance is displayed in the lower panel of Fig. 5. The comparison between the calculated periods

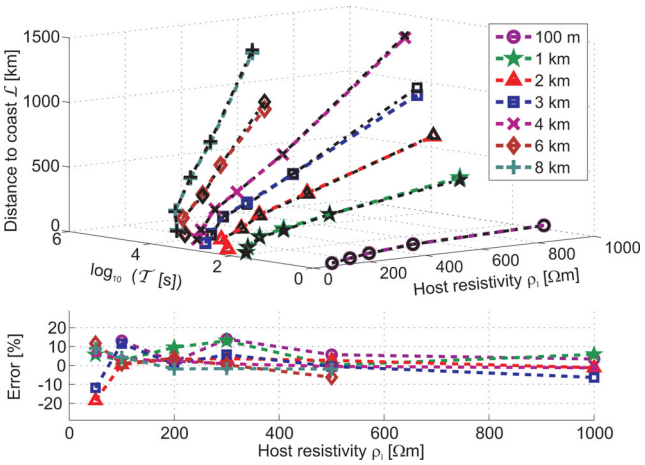

Figure 5. Check for eq. (6). Upper panel: comparison between observed and calculated characteristic distances from coast (L), dependent on the observed period and the background resistivity (observed distances are displayed in black from Table 1). Lower panel: the relative error (percentage) between calculated and observed distances L. Almost all points lie within our uncertainty in the period. Outliers are explained by an additional uncertainty due to gridding and station spacing—factors that become negligible for large distances.

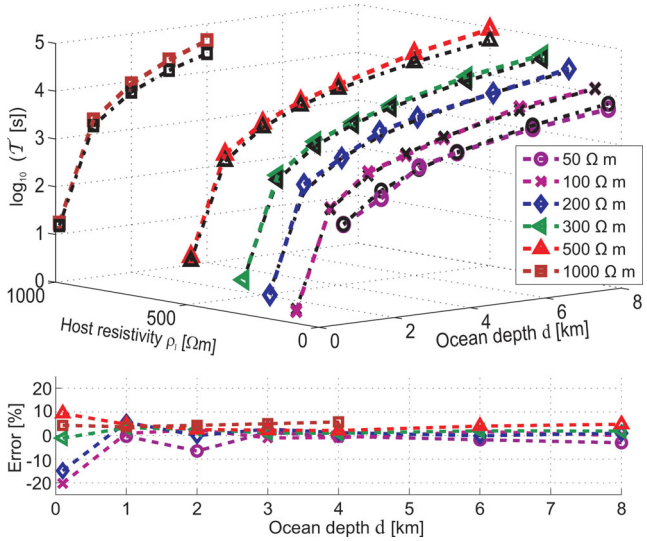

Figure 6. Check of eq. (7). Upper panel: comparison between the observed and calculated characteristic period of the maximum coast effect ($\mathcal{T}$), dependent on varying host resistivity ρ_1 and ocean depth d (observed periods in black from Table 1). Lower panel: the relative error (percentage) between calculated and observed logarithm of period $\mathcal{T}$. Almost all points lie within our uncertainty in the period.

from eq. (2) and the observed periods in Table 1 are displayed in Fig. 6. Most errors between the observed and calculated values lie within error (the uncertainty in the period or distance), so we can conclude that both equations approximate the observations well.

In reality, continental margins are not vertical, but as a first approximation may be treated as slopes. Therefore, responses of models with varying continental slope angles were also calculated using the finite difference code of Rodi & Mackie (2001) (curves not shown here). We varied the slope angle at a fixed coast position and found that the effect moves laterally with respect to the amount of water displaced. As an example: assume that the maximum coast effect is observed at distance $\mathcal{L}$ from a vertical coast. In this case, the volume of water between this distance and the coast is given by $\mathcal{L} \cdot d$. Varying the angle ϕ of continental slope without changing the position of the coast, (i.e. varying ϕ by changing the seafloor projected length of the continental slope f), we note two changes:

(1) The amount of sea water between $\mathcal{L}$ and the (vertical) coast changes (with ϕ increasing, more water is displaced with respect to a fixed reference point on the ocean bottom).

Table 1. Locations and periods of the maximum coast effect for various ocean depths and background resistivities. All models were calculated with a vertical coast. Forward models are calculated from 1 to 100 000 s with 20 periods per log-scaled decade. For a setting with low background resistivity (50 Ωm) and very shallow ocean (100 m), the maximum coast effect cannot be observed (any peak must lie within first 2 km from the coast at a period shorter than a second). At a station under a very deep ocean (>6 km) with a high resistivity host (1000 Ωm), the maximum coast effect is not observed as it theoretically should occur at a period over 100 000 s.

	Host (land) resistivity ρ_1					
Ocean-depth d	50 Ωm	100 Ωm	200 Ωm	300 Ωm	500 Ωm	1000 Ωm
100 m	(<2 km,<1 s) —	3 km 1.7 s	5 km 3 s	9 km 5 s	15 km 10 s	27 km 17 s
1 km	15 km 100 s	29 km 199 s	70 km 501 s	100 km 630 s	150 km 1122 s	300 km 1995 s
2 km	20 km 281 s	60 km 891 s	110 km 1412 s	180 km 2511 s	290 km 3981 s	590 km 8912 s
3 km	40 km 1000 s	90 km 1584 s	180 km 3981 s	260 km 5011 s	420 km 8912 s	890 km 22987 s
4 km	60 km 1584 s	110 km 2818 s	230 km 6309 s	330 km 8912 s	560 km 15 848 s	1320 km 44 668 s
6 km	90 km 3162 s	180 km 7943 s	330 km 12 589 s	520 km 22 387 s	890 km 44 668 s	– >100 000 s
8 km	110 km 5011 s	230 km 12 115 s	440 km 12 589 s	680 km 25 118 s	1310 km 39 810 s	– >100 000 s

(2) The maximum coast effect moves outwards, respectively, and is now observed at $\mathcal{L}_\phi$.

When varying ϕ from 90° to 0°, the amount of water between $\mathcal{L}$ and the coast reduces by $0.5 \cdot f \cdot d$ (the area of a right triangle area with sides d and f). This to corresponds to a shift of the new maximum coast effect by a distance of $f/2$ away from the coast, so that the new characteristic distance $\mathcal{L}_\phi$ is given as

$$\mathcal{L}_\phi = \mathcal{L} - f/2. \tag{4}$$

5 THE CHARACTERISTIC PARAMETERS AND RULES OF THUMB

The characteristic length $\mathcal{L}$ for a vertical coast is less than half of the skin depth δ in the host. Compare eq. (1) with

$$\delta \approx 0.5 \cdot \sqrt{\rho_1 \cdot T}, \tag{5}$$

where δ is in (km). One implication of this is that if the maximum coast effect is observed at a station on the ocean bottom, the coast must be accounted for during any inversion process, even at large distances. A very crude simplification of eqs (2) and (3) (using the approximation $0.95 \approx 1$ and $0.9 \approx 1$) leads to rough but simple rules of thumb

$$\text{First rule of thumb:} \quad \mathcal{T} = 3 \cdot \rho_1 \cdot d^2, \tag{6}$$

$$\text{Second rule of thumb:} \quad \mathcal{L} = \frac{1}{3} \cdot \rho_1 \cdot d, \tag{7}$$

with $\mathcal{T}$ in (s), ρ_1 in (Ωm), d in (km), $\mathcal{L}$ in (km) and for an average ocean resistivity of 0.33 Ωm.

For the case of a continental slope, when a TE mode peak in apparent resistivity is detected, one should first subtract the projected length of the slope ('f', see nomenclature in Fig. 3a) from the observed characteristic length, to estimate the host resistivity of the host, that is,

$$\mathcal{L}_{\text{used for estimation of } \rho_1} = \mathcal{L}_{\text{observed}} - f/2. \tag{8}$$

Obviously, if the underlying crust and mantle were resistive, these effects would theoretically propagate laterally over very large distances. As an example, a resistive basement of 1000 Ωm and an ocean of 4 km depth would move the maximum coast effect more than a thousand kilometres from the coast, and the highest peak in the TE mode apparent resistivity would be observable at a period of $\approx 5 \times 10^4$ s. Heinson & Constable (1992) stated that no part of the global ocean basin is immune to the distortions caused by the coast effect, which gave rise to a dispute by between Tarits *et al.* (1993) and Constable & Heinson (1993). One argument of Tarits *et al.* (1993) was that the presence of electrical connections between the ocean and deep mantle in subduction zones (and elsewhere) may have a strong effect on the MT response in the basin by reducing the influence of coast lines. The distortion of responses by the coast effect has been noted at continental margins within 200 km offshore [e.g. Constable *et al.* (2009); Wheelock *et al.* (2010) offshore California, Evans *et al.* (2010) in the Alboran Sea, Naif *et al.* (2010) offshore Nicaragua, and also in this study offshore Costa Rica]. Lilley *et al.* (1989) present coastal distorted responses of a marine station in the Tasman Sea that lie even farther offshore from any coast (their station TP1 is >500 km offshore from New Zealand island coastline and >1000 km offshore from the Australian coastline). However, distorted responses have so far not been reported on scales of thousands of kilometres away from the coastlines. If the oceanic plate were very resistive, the maximum coast effect would theoretically be transferred to large distances away from the coastlines. If one wanted to detect it, one would need very long period measurements at exactly the right spot. The question is, whether a highly resistive oceanic plate is a realistic scenario. Several measurements of the oceanic lithosphere have imaged a highly resistive lithosphere (>1000 Ωm) up to depths of around 50–150 km, which overlays a more conductive asthenospheric layer in the range of ≈1–100 Ωm; the pronounced drop in resistivity has been attributed to small contents of fluids or partial melts (summaries of oceanic lithosphere studies are included in Palshin 1996; Heinson 1999; Baba 2005). One could argue that an asthenosphere that has a high conductivity of only 1 Ωm starting at a depth of around 50 km would attenuate the incoming signal in the host too much to allow the coastal distortion to be sensed at laterally great distances.

A noteworthy observation arises when comparing the maximum coast effect in the TE mode with coastal distortion in the TM mode; electromagnetic fields in this case are characterized both by inductive and galvanic effects. The currents in the ocean that flow towards the coast (i.e. the TM mode) are deflected downwards through the seafloor because the resistive coast acts as a barrier. The zone of deflected currents in the TM mode is referred to as 'boundary zone' (Cox 1980; Lilley *et al.* 1989). Although the TM mode is not dealt with in this study, we note that Lilley *et al.* (1989) also approximate crustal resistivity by using a simplified theoretical analysis for describing the TM-mode boundary effect as introduced by Ranganayaki & Madden (1984) and Cox (1980). This approximation is given by

$$L^2_{\text{TM boundary}} = \frac{\rho_1 \cdot d \cdot H}{\rho_s}. \tag{9}$$

$L_{\text{TM boundary}}$ is the rate at which the anisotropy of the MT impedance in a coastal setting decreases with respect to its TM mode component, as the observation point moves away from the coast. In particular, $L_{\text{TM boundary}}$ describes a characteristic distance from the coast at which electric currents in the TM mode are deflected (Cox 1980; Lilley *et al.* 1989). The term $d/\rho_s = d \cdot \sigma_s$ denotes the integrated conductance of an ocean of thickness d and sea conductivity σ_s. The term $H \cdot \rho_1$ denotes the integrated host resistivity of thickness H. Eq. (9) is certainly different from the characteristic equations or rules of thumb introduced here, as it describes a different characteristic distance (the total extent of the boundary zone). However, we observe an interesting relationship between the maximum coast effect observed in TE mode and the characteristic distance of the TM mode boundary zone.

Let us approximate $\sigma_s (= 1/\rho_s)$ by 3 $\mathrm{S\,m^{-1}}$ ($= 0.33\,\Omega$m) and further, estimate the host thickness H by the extent of the induction volume, which in the homogeneous case is given by a half-sphere with radius of the skin depth (according to eq. 5)

$$H_{\text{host, skin depth}}\ (\text{km}) \approx 0.5\sqrt{T \cdot \rho_1}. \tag{10}$$

Inserting the characteristic period $\mathcal{T}$ from eq. (6) into eq. (10) and using the result in eq. (9) yields

$$L_{\text{TM boundary}} \approx 1.6 \cdot \rho_1 \cdot d \quad (\approx 5 \cdot \tfrac{1}{3} \cdot \rho_1 \cdot d). \tag{11}$$

This is the same order of magnitude as the characteristic length of the maximum coast effect in the second rule of thumb. Eqs (11) and (7) imply that the characteristic length in the TE mode lies within the boundary zone of deflected currents in the TM mode. The TM

boundary zone ends around five times farther away from the coast than where the maximum coast effect would be observed in the TE mode.

Since the maximum coast effect in the TE mode has been observed in almost all real data within 200 km from the coastlines (as listed earlier), this implies that the distortion in the TM mode responses should be observable even $5 \times 200\,\text{km} = 1000\,\text{km}$ distant from the coast.

6 AN ANALYTICAL DERIVATION OF THE TE MODE APPROXIMATIONS

A simple physical explanation of our approximations can be found using the theory of induction numbers. Consider again the 2-D model shown in Fig. 3(a), but instead of taking the ocean thickness d in units of (km), we will now express the ocean thickness as h in units of (m) to be consistent with Key & Constable (2011). The host has a resistivity ρ_1, whereas the sea water has a resistivity ρ_s and a thickness h. By definition of the TE mode, the plane wave source of period T has an electric field oriented parallel to the strike of the model. Current is then induced to flow through the ocean region in a direction parallel to the coastline. The current system has the effect of producing an anomalous magnetic field and an anomalous electric field at the seafloor. By Ampere's law, the anomalous magnetic field at the bottom of the ocean is oriented in a direction opposite to the primary magnetic field. Unlike a 1-D ocean layer, a 2-D coast model has a non-uniform distribution of current systems in the sea water. Thus, the extent to which the anomalous magnetic field destructively interferes with the primary magnetic field depends upon the specific location on the seafloor. By the definition of MT impedance, the location of the minimum total magnetic field, and consequently the location of the maximum destructive interference, will exhibit a peak in apparent resistivity.

We can estimate the location of the maximum interference of the electromagnetic fields by writing the dimensionless induction number β of a conductive target of thickness h, which represents the inductive response of the sea water, and the dimensionless induction number γ of a half-space, which represents the inductive response of the host. The reader is referred to classic works such as Grant & West (1965) for a detailed description of these induction numbers. The induction number in the host can be derived from dimensional analysis of the diffusion equation, whereas the induction number in the ocean can be derived by considering the self-inductance of a representative loop of current induced in a conductive body. For the purpose of this derivation, they are simply given as

$$\beta = \frac{\mu_0 L_s h}{\rho_s T}, \tag{12}$$

and

$$\gamma = \frac{\mu_0 L_1^2}{\rho_1 T}, \tag{13}$$

where L_s and L_1 are the characteristic length scales of induction in the sea water and the half-space, respectively. The length L_s is the size of a representative loop of current induced in the ocean, whereas the length L_1 is the physical extent of induction in the host. Complete destructive interference will only occur when the sea water and host response occur at the same frequency. Rearranging eqs (12) and (13) and equating the periods we can then write

$$\frac{h L_s}{\beta \rho_s} = \frac{L_1^2}{\gamma \rho_1}. \tag{14}$$

At a common characteristic length scale, $\mathcal{L}_{\text{analytic}} \approx L_s \approx L_1$, the maximum amount of interference will occur, resulting in a minimum total magnetic field and a peak in TE mode apparent resistivity. Solving eq. (14) for this common length scale, we find that the peak effect should occur at a characteristic distance

$$\mathcal{L}_{\text{analytic}} = b \frac{\rho_1 h}{\rho_s} \tag{15}$$

from the coast, where $b = \gamma/\beta$ and consequently is dimensionless. Substituting eq. (15) into eq. (12), we find that the peak effect should occur at a characteristic period

$$\mathcal{T}_{\text{analytic}} = a \frac{\rho_1 h^2}{\rho_s^2}, \tag{16}$$

where $a = \gamma \mu_0 / \beta^2$ and has units of magnetic permeability.

From this physical argument, the lack of a peak in the TM mode is now clear. For the TM mode, current flow in the conductive ocean is both inductive and galvanic. In addition to being described by an induction number β, the response of the conductive body is now also described by a current channelling number α, given in various works such as West & Edwards (1985) as

$$\alpha = \frac{\rho_1 h}{\rho_s L_{\text{CH}}}, \tag{17}$$

where L_{CH} is the characteristic length scale of current channeling in the sea water. There is no common characteristic distance from the coast where the physical effects of induction in the host, induction in the sea water and current channeling through the sea water occur simultaneously to produce the interference required for peak in TM mode apparent resistivity.

Substituting $\rho_s = 0.33\,\Omega\text{m}$ into eq. (15), we obtain

$$\mathcal{L}_{\text{analytic}} \approx 0.3 \cdot b \cdot \rho_1 h. \tag{18}$$

Taking the units of the ocean thickness into account, we obtain eq. (7) up to a scaling factor.

Substituting the average ocean resistivity of $\rho_s = 0.33\,\Omega\text{m}$ into eq. (16), yields

$$\mathcal{T}_{\text{analytic}} \approx 9 \cdot a \cdot \rho_1 h^2. \tag{19}$$

Taking the units of the ocean thickness into account, eq. (19) is of the same order of magnitude as eq. (6) and has the same dependence on ρ_1 and d.

Key & Constable (2011) also present empirically derived approximations which account for the peaks in TE mode apparent resistivity. Using a slightly different approach, they perform a modelling study and find that the strong peak in TE mode apparent resistivity never vanishes but instead occurs systematically at a distance of just under half a skin-length in the seafloor, in agreement with eq. (1). Furthermore, they empirically derive two equations to predict the period and range of the TE mode apparent resistivity peaks, given by

$$\mathcal{L}_{\text{Key}} = 0.091 \cdot \frac{\rho_1 h}{\rho_s}, \tag{20}$$

$$\mathcal{T}_{\text{Key}} = 1.88 \cdot 10^{-7} \cdot \frac{\rho_1 h^2}{\rho_s^2}, \tag{21}$$

where the numerical factor in front of eq. (21) has the same units as magnetic permeability. Up to a scaling constants, eqs (21) and (20) agree both in form and dimensionally with our analytically derived formulae given in eqs (15) and (16).

7 COAST EFFECTS ON SUBSURFACE ANOMALIES

Since the coast effect produces a distortion of TE mode transfer functions, it is possible that it also distorts the responses of small-scale subsurface conductivity anomalies and interferes with their detection.

Key & Constable (2011) predict an enhanced sensitivity to subsurface conductivity anomalies in the vicinity of large coastal distortion. They attribute this sensitivity to the increased flow of energy, which they express as streamlines of the Poynting vector. Let us examine this hypothesis. Consider a model consisting of three conductivity anomalies (Fig. 7a). Each conductor has a resisitivity of 10 Ωm. One conductor is located far on land, the second far offshore and the third near to the location of the maximum coast effect. We calculate the apparent resistivity and Tipper with and without these conductivity anomalies. These responses are compared by plotting their difference, as shown in Figs 7(b) and (c). The differences in responses between the anomalous model and the homogeneous model are most pronounced at the stations near the maximum coast effect. This implies that the TE mode sensitivity to conductive anomalies at depth is increased by the presence of a coastline.

Consider again the simple ocean-coast model with three anomalies. A simple test to investigate if the maximum coast effect interferes with the imaging of conductivity anomalies is shown in Fig. 8. To simulate real data, the responses are calculated with five periods per decade and 10 per cent random Gaussian noise. These responses are used in a synthetic inversion with various homogeneous starting models. We perform our inversions with WinGLink, a standard software package, which is based on the code of Rodi & Mackie (2001). We apply a smooth inversion, which seeks to solve for the smoothest model by minimizing the Laplacian of the conductivity structure. Trade-off analysis between model roughness and misfit leads to a choice of the trade-off parameter, τ, between 1 and 10.

An important condition for a successful inversion with the conjugate gradient approach is the appropriate choice of a starting model; a half-space starting model as resistive as 500 Ωm, for example, would stop after only a few iterations. Figs 8(b)–(e) display the results of the combined inversion of TM mode, Tipper and TE mode. Examples of unsuccessful inversions that became trapped in a local minimum because of inappropriate starting models are shown in Figs 8(d) and (e).

The maximum coast effect of the model with the three conductivity anomalies is observed through modelling at a station 130 km from the non-vertical coast (and 105 km from the vertical coast if the continental slope correction is performed as given in eq. 4), and at a period of 2682 s. Performing our rule of thumb and solving for the host resistivity, we obtain an average resistivity of 55 Ωm from eq. (6), and an average resistivity of 78 Ωm from eq. (7) (and 98 Ωm when the distance from coast is not corrected for the water reduction by the continental slope). As a comparison: in the model without anomalies (i.e. only ocean-coast setting and homogeneous host), the maximum coast effect is be observed at a station 140 km from the non-vertical coast (and 115 km from a vertical coast after a correction is performed according to eq. 4), and at a period of 3727 s. Performing again our rule of thumb yields a resistivity of 78 Ωm from eq. (6), and a resistivity of 86 Ωm from eq. (7) (and 105 Ωm when the distance from coast is not corrected for the water reduction by the continental slope).

These results suggest that applying our rules of thumb for guessing the host resistivity of the model with anomalies may serve for an appropriate choice of starting model. This is shown in Figs 8(b) and

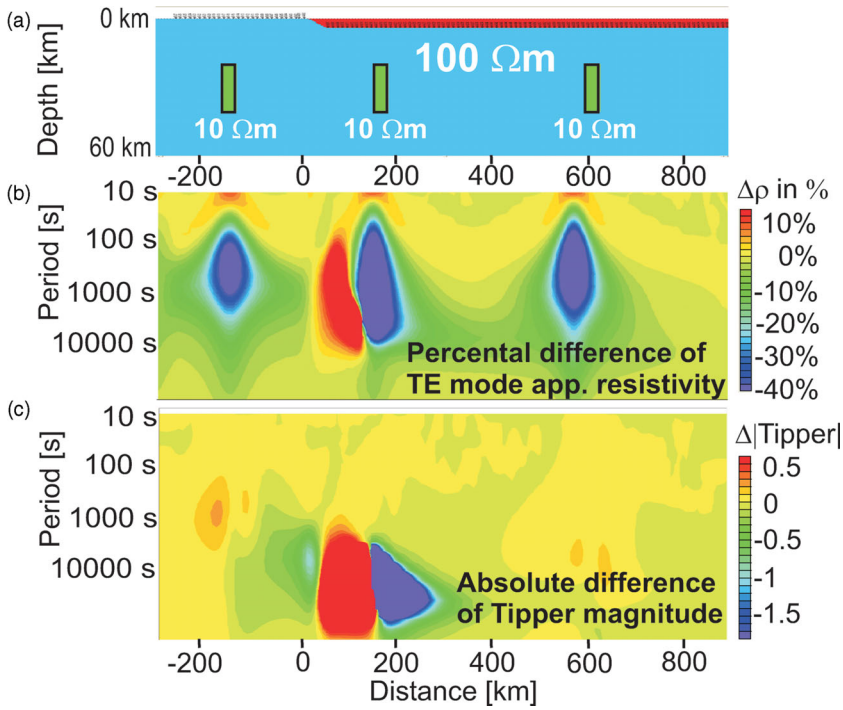

Figure 7. Comparison of the TE mode and Tipper sensitivity to conductivity anomalies. (a) Anomalous model containing three conductors, each with a resistivity of 10 Ωm. In the following panels, responses of this model are compared with responses of the homogeneous case (without anomalies). (b) Difference (per cent) in the TE mode apparent resistivity. (c) Absolute difference of Tipper magnitude. The conductivity anomaly in the vicinity of the maximum coast effect produces the greatest difference in the responses.

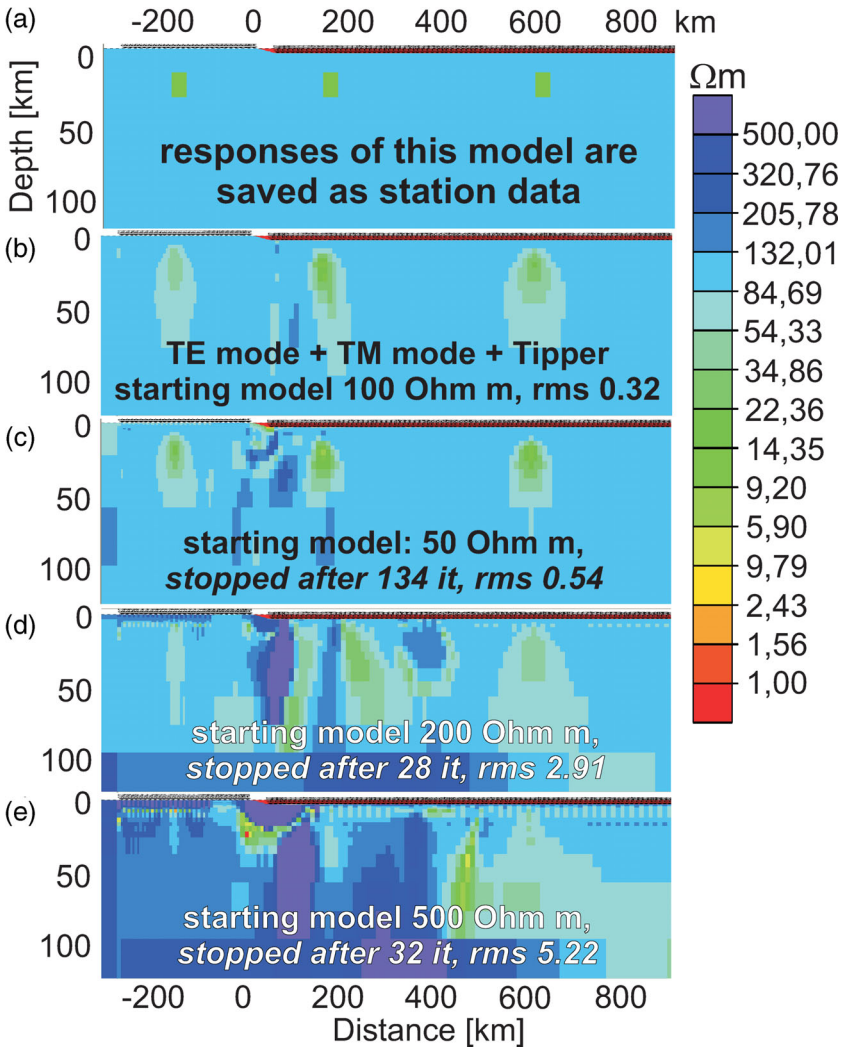

Figure 8. Inversion of conductivity anomalies under different conditions. The responses of the model in the uppermost panel (a) are saved as station data. Several inversions are performed with a homogeneous half-space and a fixed ocean included in the starting model. Different starting model resistivities are chosen in panels (b)–(e). Please note that an rms smaller 1 is explained by the fact that we artificially added 60 per cent error bars the TE mode phase data. This is because our particular version of the inversion software WinGlink cannot handle phases progressing through four quadrants. Consequently, we had to de-emphasize the TE mode phases to achieve a convergence of the inversion process. For further discussion see text.

(c). Both inversions, one with 100 Ωm and the one with 50 Ωm as starting background resistivities, resolve the conductivity anomalies well.

An alternative solution is to use the Occam inversion by Constable *et al.* (1987), since Constable *et al.* (2009) do not report on any problems with the choice of starting models. This suggests that the sensitivity of our inversion to the particular starting model could lie in the nature of the conjugate gradient approach. However, the results of this section show that our rules of thumb can be used to overcome this particular limitation.

8 CONCLUSIONS

The 2-D marine coast effect has a unique and specific nature: The distortion in the TE mode and the Tipper is maximized at a characteristic distance from a vertical coast at a characteristic period. This effect is defined here as the maximum coast effect. Numerical modelling reveals that the characteristic distance from a vertical coast approximately depends on the product of host (land) resistivity and ocean depth. The characteristic period approximately depends on the product of host resistivity and the square of the ocean depth. Similar relationships are introduced in a recent publication by Key & Constable (2011). However, we provide a simple physical explanation of these approximations by showing that the maximum coast effect occurs when the destructive interference between the ocean and host response is at its highest. The coast effect does not hamper the detection of subsurface conductivity anomalies; in fact the sensitivity to conductive structures is enhanced for stations in the vicinity of the maximum distortion. If the coast is modelled with a continental slope instead of a vertical boundary, the position of the maximum coast effect moves according to the modelled change in water volume. Since a deep ocean combined with a high host resistivity may allow the distortion to theoretically propagate over very large distances, special care must be taken when inverting marine data at continental margins. Due to the localized nature of the maximum coast effect, a dense coverage of marine stations is

essential for detection. The approximations presented here may be used to find an appropriate starting model for an inversion of marine MT data. Future work will focus on 3-D modelling studies to test the dependency of sea water volume on the distortion of MT and magnetic transfer functions.

ACKNOWLEDGMENTS

This publication is contribution no. 218 of the Sonderforschungsbereich 574 'Volatiles and Fluids in Subduction Zones' at Kiel University and IFM-GEOMAR. Thanks goes to Antje Franke for providing her code for the numerical modelling. We also like to acknowledge Martin Thorwart, Anna Avdeeva, Max Moorkamp, Heinrich Brasse and Gerhard Kapinos for inspiring discussions and important contributions to this study. We would like to thank Rob Evans and an anonymous reviewer for their thoughtful reviews which have helped to improve this paper.

REFERENCES

Alekseev, D.A., Palshin, N.A. & Varentsov, I.M., 2009. Magnetotelluric dispersion relations in a two-dimensional model of the coastal effect, *Phys. Solid Earth,* **45**(2), 167–170.

Baba, K., 2005. Electrical structure in tectonic settings, *Surv. Geophys.,* **26,** 701–731.

Baba, K. & Chave, A.D., 2005. Correction of seafloor magnetotelluric data for topographic effects during inversion, *J. geophys. Res.,* **110**(B12105), 1–16.

Baba, K. & Seama, N., 2002. A new technique for the incorporation of seafloor topography in electromagnetic modelling, *Geophys. J. Int.,* **150,** 392–402.

Constable, S. & Heinson, G., 1993. In defence of a resistive oceanic upper mantle: reply to a Comment by Tarits, Chave and Schultz, *Geophys. J. Int.,* **52**(3), 289–300.

Constable, S., Key, K. & Lewis, L., 2009. Mapping offshore sedimentary structure using electromagnetic methods and terrain effects in marine magnetotelluric data, *Geophys. J. Int.,* **176,** 431–442.

Constable, S.C., Parker, R.L. & Constable, C.G., 1987. Occam's inversion—a practical algorithm for generating smooth models from electromagnetic sounding data, *Geophysics,* **52**(3), 289–300.

Cox, C.S., 1980. Electromagnetic induction in the oceans and inferences on the constitution of the Earth, *Geophysics,* **4,** 137–156.

Evans, R.L., Jegen, M., Garcia, X.A., Matsumo, T., Elsenbeck, J. & Worzewski, T., 2010. Magnetotelluric measurements in the Alboran Sea, *Proc. 2010 Fall Meeting, AGU,* Abstract T23C-2284.

Ferguson, I.J., 1988. The Tasman Project of seafloor magnetotelluric exploration, *Ph.D. thesis*, Australian National University.

Ferguson, I.J., Lilley, F.E.M. & Filloux, J.H., 1990. Geomagnetic induction in the Tasman Sea and electrical conductivity structure beneath the Tasman Seafloor, *Geophys. J. Int.,* **102,** 299–312.

Franke, A., Börner, R.U. & Spitzer, K., 2007. Adaptive unstructured grid finite element simulation of two-dimensional magnetotelluric fields for arbitrary surface and seafloor topography, *Geophys. J. Int.,* **171,** 71–86.

Grant, F.S. & West, G.F., 1965. *Interpretation Theory in Applied Geophysics,* McGraw-Hill, New York, NY.

Heinson, G., 1999. Electromagnetic studies of the lithosphere and asthenosphere, *Surv. Geophys.,* **20,** 229–255.

Heinson, G. & Constable, S., 1992. The electrical conductivity of the oceanic upper mantle, *Geophys. J. Int.,* **110,** 159–179.

Heinson, G. & Lilley, F.E.M., 1993. An application of thin-sheet electromagnetic modelling to the Tasman Sea, *Phys. Earth planet. Inter.,* **81,** 231–252.

Hobbs, B.A., 1992. Terminology and symbols for use in studies of electromagnetic induction in the Earth, *Surv. Geophys.,* **13,** 489–516.

Kellet, R., Lilley, F.E.M. & White, A., 1991. A two-dimensional interpretation of the geomagnetic coast effect of southeast Australia, observed on land and seafloor, *Tectonophysics,* **192,** 367–382.

Key, K. & Constable, S., 2011. Coast effect distortion of marine magnetotelluric data: insights from a pilot study offshore northeastern Japan, *Phys. Earth planet. Inter.,* **184,** 194–207.

Lilley, F.E.M., Filloux, J.H., Ferguson, I.J., Bindoff, N.L. & Mulhearn, P.J., 1989. The Tasman project of seafloor magnetotelluric exploration: experiment and observations, *Phys. Earth planet. Inter.,* **53,** 405–421.

Naif, S., Key, K.W., Constable, C. & Evans, R.L., 2010. First results from SERPENT marine MT study, *Proc. 2010 Fall Meeting, AGU,* Abstract GP21B-07.

Nolasco, J., Tarits, P., Filloux, J.H. & Chave, A.D., 1998. Magnetotelluric imaging of the Society Isalnds hotspot, *J. geophys. Res.,* **103,** 30 287–30 309.

Palshin, N.A., 1996. Oceanic electromagnetic studies: a review, *Surv. Geophys.,* **17,** 455–491.

Ranganayaki, R.P. & Madden, T.R., 1984. Generalized thin sheet analysis in magnetotellurics: an extension of Price's analysis, *Geophys. J. Int.,* **60,** 445–457.

Rodi, W. & Mackie, R.L., 2001. Nonlinear conjugate gradients algorithm for 2-D magnetotelluric inversion, *Geophysics,* **66,** 174–187.

Schwalenberg, K. & Edwards, R.N., 2004. The effect of seafloor topography on magnetotelluric fields: an analytical formulation confirmed with numerical results, *Geophys. J. Int.,* **159,** 607–621.

Tarits, P., Chave, A.D. & Schultz, A., 1993. Comment on 'The electrical conductivity of the oceanic upper mantle' by G. Heinson and S. Constable., *Geophys. J. Int.,* **114,** 711–716.

West, G.F. & Edwards, R.N., 1985. A simple parametric model for the electromagnetic response of an anomalous body in a host medium, *Geophysics,* **50,** 2542–2557.

Wheelock, B., Constable, S. & Key, K., 2010. A marine electromagnetic study of the continental margin in central California, USA, *20th Electromagnetic Induction Workshop* Giza, Egypt, 2010 September 18–24, extended abstract.

Worzewski, T. & Jegen-Kulcsar, M., 2010. The coastal effect on marine MT data: determining a characteristic period & characteristic length to account for peaks in TE mode apparent resistivity, negative phases and an unusual Tipper, *20th Electromagnetic Induction Workshop* Giza, Egypt, 2010 September 18–24, extended abstract.

Worzewski, T., Jegen, M., Kopp, H., Brasse, H. & Taylor, W., 2011. Magnetotelluric image of the fluid cycle in the Costa Rican subduction zone, *Nature Geosci.,* **4**(2), 108–111.

APPENDIX

Some notes should be made to clarify the expression 'Tipper'. In this paper, the Tipper is a synonym for the magnetic transfer function (in accordance to Hobbs 1992), which is a vector that relates the horizontal magnetic field (H_x, H_y) to the vertical magnetic field H_z. The Tipper is defined via the equation

$$(Tip_x, Tip_y) \cdot (H_x, H_y) = H_z,$$

where Tip_x and Tip_y are the two complex valued components. The Tipper is sometimes graphically presented by real and imaginary induction arrows, which are constructed from the real and imaginary parts of each component (Re[Tip_x], Re[Tip_y]) and (Im[Tip_x], Im[Tip_y]). The magnitude of the Tipper is given by

$$\begin{aligned} \mathrm{abs}[Tipper] &= \sqrt{Tip_x \cdot Tip_x^* + Tip_y \cdot Tip_y^*} \\ &= \sqrt{\mathrm{Re}[Tip_x]^2 + \mathrm{Im}[Tip_x]^2 + \mathrm{Re}[Tip_y]^2 + \mathrm{Im}[Tip_y]^2}, \end{aligned}$$

where superscript $*$ denotes the conjugate of the complex number.

For a 2-D setting with H_x aligned parallel to the 2-D strike direction and H_y perpendicular to strike, Tip_x turns zero and Tip_y

depends on the conductivity contrast. In this study, a 2-D situation is provided by a simple ocean-coast setting, where H_x is aligned parallel to the coastline and with the profile oriented perpendicular to the coast. Therefore, the Tipper in this setting only consists of its complex value Tip_y given by $H_z \cdot H_y^{-1}$, which in this paper is expressed either by its real and imaginary components, $\mathrm{Re}[Tip_y]$ and $\mathrm{Im}[Tip_y]$, or is expressed by its magnitude $\mathrm{abs}[Tipper] = \sqrt{\mathrm{Re}[Tip_y]^2 + \mathrm{Im}[Tip_y]^2}$. In this paper, the Tipper subscripts are discarded for simplification, as the Tipper corresponds to the remaining non-zero complex component Tip_y.